arXiv:astro-ph/0205103v1 7 May 2002

Fast Reconnection in a Two-Stage Process

Fabian Heitsch[1]

Ellen G. Zweibel[1]

submitted to ApJ

ABSTRACT

Magnetic reconnection plays an essential role in the generation and evolution of astrophysical magnetic fields. The best tested and most robust reconnection theory is that of Parker and Sweet. According to this theory, the reconnection rate scales with magnetic diffusivity λ_Ω as $\lambda_\Omega^{1/2}$. In the interstellar medium, the Parker-Sweet reconnection rate is far too slow to be of interest. Thus, a mechanism for fast reconnection seems to be required. We have studied the magnetic merging of two oppositely directed flux systems in weakly ionized, but highly conducting, compressible gas. In such systems, ambipolar diffusion steepens the magnetic profile, leading to a thin current sheet. If the ion pressure is small enough, and the recombination of ions is fast enough, the resulting rate of magnetic merging is fast, and independent of λ_Ω. Slow recombination or sufficiently large ion pressure leads to slower merging which scales with λ_Ω as $\lambda_\Omega^{1/2}$. We derive a criterion for distinguishing these two regimes, and discuss applications to the weakly ionized ISM and to protoplanetary accretion disks.

Subject headings: conduction — diffusion — ISM:magnetic fields — MHD

1. Outline of the Problem

The Ohmic diffusion time scale in the interstellar medium (ISM) is so long compared to the dynamical time scale that at first sight the magnetic field would appear to be perfectly frozen to the plasma. The ratio of these two time scales, – the Lundquist number S – is typically $10^{15} < S < 10^{21}$, implying Ohmic diffusion times much longer than the age of the universe.

The weakness of Ohmic diffusion causes serious problems for Galactic dynamo theory, which requires breaking the frozen-flux condition in order to convert small scale fields to large scale fields. More generally, it is difficult to reconcile the frozen-flux condition with the apparent smoothness of the magnetic field in the ISM and the apparently turbulent nature of the interstellar velocity field.

Magnetic reconnection is a "hybrid" process which combines resistive and dynamical effects, and acts at a rate intermediate between them. When the reconnection rate depends on S (usually a power-law dependence), it is said to be slow. Fast reconnection, by definition, proceeds at a rate independent of S. It is generally accepted that in order for reconnection to cause a substantial breakdown of flux freezing in the ISM, it must be fast.

The reconnection theories of Parker (1957) and Sweet (1958) have proven durable, and represent in some sense the "default" models, to which later work is usually compared. In the Parker-Sweet models, two opposing magnetic field systems are pressed together, forming a current sheet at the magnetic null plane at which the field undergoes steady state, resistive annihilation. According to

[1]JILA, University of Colorado, Campus Box 440, Boulder, CO 80309-0440, USA

this model, the reconnection rate scales as $S^{1/2}$.

Petschek (1964) argued for changing the geometrical setup from reconnection in a current sheet to an X-point geometry. In this model, the reconnection rate is proportional to $(\ln S)^{-1}$. However, both numerical (Cowley 1975; Biskamp 1986; Scholer 1989; Biskamp 1994; Ugai 1995) and analytical studies (Kulsrud 1998, 2001) cast doubt on whether Petschek's model is realizable, unless special conditions are met (Forbes 2001). Another solution based on flow geometry was proposed by Lazarian & Vishniac (1999), who argued that fast reconnection occurs in the presence of turbulence at the resistive length scale; see also Chiueh & Zweibel (1989).

The solution to the fast reconnection problem could lie in physical processes outside the scope of single-fluid magnetohydrodynamics. The high electric current density expected in the reconnection layer may lead to instabilities which could generate small scale electromagnetic or electrostatic turbulence. Scattering of electrons by such turbulence provides so-called anomalous resistivity (see Treumann (2001) and references therein) and increases the reconnection rate. If the current layers are sufficiently thin, electrons and ions may decouple (Mandt et al. 1994). As Biskamp et al. (1995) argue, this can lead to reconnection at a rate independent of the resistivity.

Dorman & Kulsrud (1995) showed that the reconnection layer can be made thin if the gas pressure is reduced by progressive cooling. They found that a resistive region will form within a cooling time multiplied by $\ln S$, and that the magnetic field is dissipated within a few subsequent cooling times. However, as they argue, the temperature must be reduced by a factor of $S^{1/4}$ for this to happen. Bearing in mind the value of S in the ISM, the study demonstrates very clearly *how* large S actually is.

In this paper, we consider ambipolar diffusion (Mestel & Spitzer 1956) as a mechanism to reduce the reconnection layer width. Zweibel (1989) investigated the effect of partial ionization on tearing instabilities in a sheared magnetic field. The reconnection rate is increased by a factor of $(\rho/\rho_i)^{1/5}$, but the $S^{3/5}$-dependence found in the theory of Furth et al. (1963) is unchanged. Vishniac & Lazarian (1999) considered Parker-Sweet reconnection in weakly ionized gas. They argued that although the rate remains proportional to $S^{1/2}$, it can be enhanced by several orders of magnitude due to recombination of ions in the resistive layer. Brandenburg & Zweibel (1994) showed that ambipolar diffusion steepens the magnetic profile in the vicinity of a magnetic null layer, and suggested that the resulting high current density could set the stage for magnetic reconnection. Brandenburg & Zweibel (1995) – hereafter BZ95 – found that although ion pressure tends to broaden the resistive layer and reduce the reconnection rate, a fast reconnection regime exists that is accessible under ISM conditions.

This paper is in some respects a followup of BZ95. We consider the steady state properties of a layer of weakly ionized gas around a field reversal, with the magnetic field fixed at the outer boundaries. We show by analytical arguments and a set of numerical models, that magnetic merging can be either fast or slow. The merging rate depends on a single parameter combining the ratio β of ion pressure to magnetic pressure, the Ohmic diffusivity λ_Ω, the ambipolar diffusivity λ_{AD}, the recombination rate of ions, and the global length scale L in the problem. Our result suggests that fast merging of magnetic neutral sheets is possible in the weakly ionized interstellar gas.

In §2 we define the problem, quantify the relevant time scales, and develop an analytical model for predicting the reconnection rates. A numerical solution of the problem requires a solver which is able to handle the disparate time scales; we describe the solver in §3. In §4, the numerical results are analyzed and compared with the analytical theory. We discuss the implications for the ISM in §5. Section 6 is a summary and discussion.

2. Analytical Description

Before embarking on a mathematical representation of the problem, we describe the physical setup and identify the critical parameters which we would like to determine.

We begin by summarizing reconnection theory of Parker (1957) and Sweet (1958), the main features of which have been confirmed by many subsequent calculations (e.g. Biskamp (1993); Uzdensky & Kulsrud (2000)). The basic configuration is sketched in Figure 1, in the coordinate system which we will use throughout this paper.

Opposing fields $\pm\hat{y}B_0$ are pressed together over a

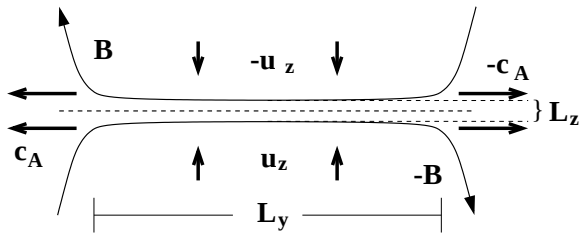

Fig. 1.— Configuration for steady state reconnection according to Parker-Sweet theory.

length L_y, leading to a current sheet of width L_z centered on $z = 0$. Resistive dissipation of the current annihilates the field. In a steady state, magnetic flux must be brought in at the boundaries at the rate at which it is destroyed. The reconnection rate is parameterized by the speed u_z at which the field is convected inwards, and determining this inflow speed in terms of the geometrical parameter L_y and the intrinsic plasma parameters is one of the central problems of reconnection theory.

In Parker-Sweet theory, u_z is determined as follows. The electric field $\mathbf{E}$ is assumed to be given by the standard MHD form of Ohm's law

$$\mathbf{E} = -\frac{\mathbf{u}\times\mathbf{B}}{c} + \frac{\mathbf{J}}{\sigma}, \tag{1}$$

where σ is the electrical conductivity. In the present problem, $\mathbf{E} = \hat{x}E$ must be constant, because the system is in a steady state. We approximate $\mathbf{E}$ by its inductive value $-\mathbf{u}\times\mathbf{B}/c$ everywhere except in the resistive region, where we approximate it by the expression $\mathbf{J}/\sigma$. Equating the resistive and inductive expressions for $\mathbf{E}$, and using Ampère's law to write $\mathbf{J}$ as $\hat{x}cB_0/(4\pi L_z)$, we find

$$L_z = \frac{\lambda_\Omega}{u_z}, \tag{2}$$

where $\lambda_\Omega \equiv c^2/(4\pi\sigma)$ is the magnetic diffusivity.

A second relationship between L_z and u_z follows from conservation of mass. The inward mass flux $\rho u_z L_y$ must be balanced by outward mass flux in the form of thin jets within the resistive layer. Energy conservation arguments suggest that these jets travel at the Alfvén speed $c_\mathrm{A} \equiv B_0/(4\pi\rho)^{1/2}$, implying an outward mass flux $\rho c_\mathrm{A} L_z$. Equating the inward and outward mass fluxes yields

$$L_z = L_y\frac{u_z}{c_\mathrm{A}}. \tag{3}$$

Combining equations (2) and (3) yields expressions for u_z and L_z

$$u_z = \left(\frac{\lambda_\Omega c_\mathrm{A}}{L_y}\right)^{1/2} = c_\mathrm{A}S^{-1/2}, \tag{4}$$

$$L_z = \left(\frac{\lambda_\Omega L_y}{c_\mathrm{A}}\right)^{1/2} = L_y S^{-1/2}, \tag{5}$$

where the Lundquist number S is defined as

$$S \equiv \frac{\tau_\Omega}{\tau_\mathrm{A}} = \frac{L_y\, c_\mathrm{A}}{\lambda_\Omega}. \tag{6}$$

In the interstellar medium, S is generally enormous (quantitative estimates follow in §2.2), while the Alfvén crossing time is comparable to the dynamical time. Equation (4) therefore implies that reconnection is very slow.

In this paper, we express the reconnection rate in terms of the electric field. In Parker-Sweet reconnection, E is given by

$$E = \frac{u_z B_0}{c} = \left(\frac{\lambda_\Omega c_\mathrm{A}}{L_y}\right)^{1/2}\frac{B_0}{c}, \tag{7}$$

where we have used equation (4). The relations (4) and (5) imply that the Ohmic heating rate $\dot{e}_{mag}$ per unit volume is independent of λ_Ω

$$\dot{e}_{mag} = \frac{4\pi\lambda_\Omega}{c^2}\mathbf{J}^2 = \frac{c^2}{4\pi\lambda_\Omega}\mathbf{E}^2, \tag{8}$$

where the second equality holds only in the resistive region. The Poynting flux into the region, $u_z B_0^2/(4\pi)$, is proportional to $\lambda_\Omega^{1/2}$.

We now consider the problem in weakly ionized gas. Again, we assume a reversal in $\hat{y}B(z)$ at $z = 0$. When the charged and neutral matter are strongly coupled, regions of magnetic field reversal can achieve force balance, with neutral pressure compensating for the deficit in magnetic pressure. Reducing the coupling between neutrals and ions leads to ambipolar diffusion, in which case the neutrals lag behind the field lines. Neutral pressure support is lost, and the ion pressure – which is much smaller than the neutral pressure – is overwhelmed by the magnetic pressure squeezing the

antiparallel field lines together. The magnetic field gradients steepen around the magnetic null, leading to high current densities and Ohmic dissipation. The basic situation is sketched in Figure 2.

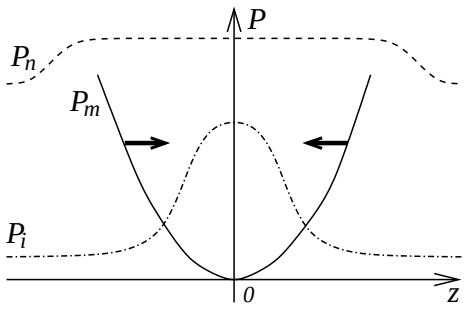

Fig. 2.— Sketch of magnetic (P_m), ion (P_i) and neutral pressure (P_n) around the resistive region at $z = 0$. The magnetic field strength B would increase linearly. The neutral pressure is much larger than any other pressure. The magnetic pressure squeezes the antiparallel field lines together, only resisted by the ion pressure.

An important simplification of the Parker-Sweet problem arises because the flux of ions is not conserved. Recombination represents a sink, thus eliminating the need for an outflow and making a steady state possible in one dimension. Although the system could develop 2D or 3D structure - and, as we discuss in §6 this may be the only way to achieve fast reconnection under certain conditions - we treat only the 1D case here, because it is simplest and most tractable. In the spirit of our discussion of Parker-Sweet reconnection, we are interested in finding the scaling of the steady state inflow speed, or equivalently the electric field, with the Ohmic diffusivity λ_Ω.

In §2.1, we write down the basic equations which govern the system. In §2.2, we nondimensionalize the problem and define and estimate the important basic time scales. In §2.3 we derive the reconnection rate assuming ionization equilibrium is maintained at all times, and in §2.4 we derive scaling relations for the inflow velocity and layer thickness when the recombination rate is high but finite.

2.1. Basic Equations

BZ95 solved the time dependent layer problem for two fluids, one charged and the other neutral, which are coupled by elastic collisions and by ionization and recombination. In the parameter regime of interest, they found that the problem is adequately described by a reduced set of steady state equations for the ions. We have generalized these equations to allow for a polytropic equation of state, $P_i \propto \rho_i^\gamma$, instead of the isothermal relation assumed in BZ95. The dynamics of the neutrals are neglected, because the neutrals are not coupled to the magnetic field and their pressure profile is essentially flat (see Fig. 3 of BZ95). The ionization fraction is sufficiently small that the neutrals can be regarded as an infinite reservoir which can be supplemented by recombination with negligible effect on its overall properties. The ion flow is assumed slow enough that ion inertia can also be neglected. As we will see, this imposes a constraint on the width L of the layers that can be described by these reduced equations.

The magnetic induction equation, the ion momentum equation, and the ion continuity equation are

$$\frac{\partial}{\partial z}\left(u_i B - \lambda_\Omega \frac{\partial}{\partial z} B\right) = 0 \quad (9)$$

$$\frac{\partial}{\partial z}\left(2\rho_{i0} c_{i0}^2 \left(\frac{\rho_i}{\rho_{i0}}\right)^\gamma + \frac{B^2}{8\pi}\right) + \rho_i \nu_{in} u_i = 0 \quad (10)$$

$$\frac{\partial}{\partial z}\left(\rho_i u_i\right) - R_i \rho_{n0} + R_{rec} \rho_i^2 = 0 \quad (11)$$

Table 1 explains the variables. The symbols R_i and R_{rec} denote the ionization rate per unit time and the recombination rate per charged particle, respectively. Equation (11) is valid for photoionization or cosmic ray ionization, and for radiative or dissociative recombination, but not for surface recombination on grains, unless the grains are tied to the ions rather than the neutrals. Equation (9) can be integrated to yield

$$u_i B - \lambda_\Omega \frac{\partial}{\partial z} B = -cE, \quad (12)$$

and we will always use it in this form.

Equations (10), (11), and (12) are solved on the domain $0 \le z \le L$, with symmetry assumed about $z = 0$. The subscripts "0" denote conditions at $z = L$. The boundary values at $z = 0$ are

$B(0) = 0$, $u_i(0) = 0$. We also impose the conditions $B(L) = B_0$ and $\rho_i(L) = \rho_{i0}$. We are able to impose a fourth condition in a system of three first order ordinary differential equations (ODEs) by treating E as an eigenvalue.

For $\lambda_\Omega \to 0$ the order of equation (12) changes. Thus, we expect two physically distinct regions, namely a resistive region around $z = 0$ where $\lambda_\Omega \partial B/\partial z$ dominates, and an inductive region for $z \gg 0$ governed by the inductive term $u_i B$, just as occurs in the Parker-Sweet solution.

2.2. Dimensionless Formulation and Time Scales

As the problem is largely one of time scale ratios, we rewrite equations (10) - (12) in a dimensionless form with the relevant time scales as physical parameters. We scale the physical variables as in Table 1, and introduce the time scales in Table 2. We also define the β parameter

$$\beta \equiv \frac{16\pi c_{i0}^2 \rho_{i0}}{B_0^2}. \tag{13}$$

The factor of 2 in equation (13) accounts for electron pressure, which we assume to be the same as the ion pressure.

We assume ionization equilibrium at the outer boundary, such that $\tau_{rec} = \tau_i$. Rewriting the reduced equations as a set of first order ODEs for each variable and using equation (13) and Table 2 we find

$$\frac{\partial}{\partial x} b = \tau_\Omega \left(\frac{1}{\tau_{ind}} + \frac{1}{\tau_A} v b \right) \tag{14}$$

$$\frac{\partial}{\partial x} r = -\frac{2}{\beta\gamma} r^{1-\gamma} \left(b \frac{\partial}{\partial x} b + \frac{\tau_{AD}}{\tau_A} r v \right) \tag{15}$$

$$\frac{\partial}{\partial x} v = \frac{\tau_A}{\tau_i} \frac{1}{r} (1 - r^2) - \frac{v}{r} \frac{\partial}{\partial x} r. \tag{16}$$

Note that the time scales occur only as ratios, and that they depend on the length scale L in different ways: τ_i is independent of L, τ_A is linearly proportional to L, and τ_{AD} and τ_Ω are proportional to L^2. Thus, for example, the ratio τ_Ω/τ_{AD} is fixed in terms of the intrinsic parameters of the medium, but the ratio of either one to τ_i can be made larger or smaller by appropriate choice of L.

Physical realism dictates certain constraints on the time scales, which are discussed in the following subsections.

2.2.1. The resistive time scale τ_Ω

The magnetic diffusivity λ_Ω is related to the conductivity perpendicular to the magnetic field $\sigma_\perp$ by

$$\lambda_\Omega = \frac{c^2}{4\pi\sigma_\perp}. \tag{17}$$

Braginskii (1965) gives $\sigma_\perp$ in terms of the electron collision time τ_e as

$$\sigma_\perp = \frac{n_e e^2 \tau_e}{m_e}. \tag{18}$$

Electrons collide with both charged and neutral species, at rates which we denote by τ_{ei}^{-1} and τ_{en}^{-1}, respectively. Combining the effects of collisions of both types leads to the composite expression

$$\tau_e = \frac{\tau_{ei}\tau_{en}}{\tau_{ei} + \tau_{en}}. \tag{19}$$

We evaluate τ_{ei} from Braginskii (1965) with a mean ion charge Z equal to unity, and the Coulomb logarithm Λ set equal to 20. We evaluate τ_{en} for H_2 as the primary neutral species, using the rates given by Draine et al. (1983). The result is

$$\tau_e = \frac{1.4 \times 10^{-2} T^{3/2}}{n_e \left[1 + 1.2 \times 10^{-11} T^2 x_i^{-1}\right]} \text{ [s]}, \tag{20}$$

with the ionization fraction $x_i \equiv n_e/n_n$. Electron-neutral collisions are represented by the second term in square brackets in the denominator of equation (20). Such collisions are ignorable in most of the environments considered in this paper. However, under the conditions found in protoplanetary disks, they dominate over electron-ion collisions.

Equations (17), (18), and (20) combine to give the magnetic diffusivity

$$\lambda_\Omega = \frac{2.0 \times 10^{13}}{T^{3/2}} \left[1 + 1.2 \times 10^{-11} T^2 x_i^{-1}\right] \text{ [cm}^2 \text{ s}^{-1}\text{]}. \tag{21}$$

The Ohmic diffusion time τ_Ω (see Table 1) is then given by

$$\tau_\Omega = 1.54 \times 10^{16} L_{\rm pc}^2 \frac{T^{3/2}}{\left[1 + 1.2 \times 10^{-11} T^2 x_i^{-1}\right]} \text{ [yrs]}. \tag{22}$$

2.2.2. The ambipolar diffusion time scale τ_{AD}

The ambipolar diffusivity λ_{AD} depends on the field strength B, the particle number densities n_i, n_n, the molecular weights μ_i and μ_n (we assume a single species of each), the ionization fraction $x_i = n_i/n_n$, and the rate coefficient for elastic collisions $\langle\sigma v\rangle$. We write

$$\begin{aligned}\lambda_{AD} &= \frac{(\mu_i+\mu_n)}{4\pi\langle\sigma v\rangle\mu_i\mu_n m_H x_i}\left(\frac{B}{n_n}\right)^2 \\ &= 3.2\times10^{31}\frac{(\mu_i+\mu_n)}{\mu_i\mu_n x_i}\left(\frac{B}{n_n}\right)^2\ [\mathrm{cm^2\,s^{-1}}],\end{aligned} \tag{23}$$

where we have taken $\langle\sigma v\rangle = 1.5\times10^{-9}\mathrm{cm^3 s^{-1}}$ (Draine et al. 1983). Thus, the ambipolar diffusion time scale is (see Table 1)

$$\tau_{AD} = 9.4\times10^{-3}\,L_{\rm pc}^2\left(\frac{n_n}{B}\right)^2\frac{\mu_i\mu_n x_i}{(\mu_i+\mu_n)}\ [\mathrm{yrs}]. \tag{24}$$

2.2.3. The ionization time scale τ_i

We assume ionization equilibrium at the outer boundary so that $\tau_{rec} = \tau_i$. Significant departures from ionization equilibrium are always in the sense of a surplus of ions, so it is the recombination rates which matter. We summarize them here.

Following Draine & Sutin (1987) and McKee (1989), we assume that molecular ions are destroyed primarily by dissociative recombination, while atomic ions undergo radiative recombination, and also recombine on the surfaces of dust grains. Denoting the rate coefficients for these three processes by α_{dr}, α_{gr}, and α_{rr}, respectively, we write the total recombination rate R_{rec} as

$$R_{rec} = (\mu_i m_H)^{-1}\left[\phi\alpha_{dr} + (1-\phi)\alpha_{rr} + \alpha_{gr}x_i^{-1}\right], \tag{25}$$

where $\phi \equiv 0$ for atomic ions and $\phi \equiv 1$ for molecular ions. The recombination time including all three processes is then given by

$$\tau_{rec} = (R_{rec}\rho_i)^{-1}. \tag{26}$$

Equation (25) is valid when the grain density follows the neutral density. As such, it is inconsistent with equation (11), because the rate of recombination on negatively charged grains is then linear in the ion density rather than quadratic. We have not included this possibility in our calculations, but we comment on it in §6. It is possible that at least some of the grains follow the ions; see Ciolek & Mouschovias (1993) for a discussion of grain-gas coupling.

Taking expressions for the α coefficients from Draine & Sutin (1987), we have

$$\alpha_{rr} = \frac{7.2\times10^{-11}}{T^{1/2}} \tag{27}$$

$$\alpha_{dr} = 1.4\times10^{-5}\,T^{-3/4} \tag{28}$$

$$\alpha_{gr} = \frac{2.9\times10^{-12}}{(\mu_i T)^{1/2}}\left(\frac{3\text{Å}}{a_{min}}\right)^{3/2}, \tag{29}$$

all in units of $\mathrm{cm^3 s^{-1}}$. In equations (29), a_{min} is the minimum grain size, with the size spectrum assumed to follow the MRN power law (Mathis et al. 1977). For the numbers given in Table 3, we used $a_{min} = 3$ Å. Although this value of a_{min} is uncertain, our final results are rather insensitive to it, because of the relatively large coefficients of radiative and dissociative recombination.

2.2.4. The Alfvén crossing time τ_A

The non-dimensionalization leaves us with a "crossing time" in the problem. There are various ways to define this crossing time. As it is not clear what the velocity at the outer boundary will be (see below as well), but values for the magnetic field B_0 and the density ρ_{i0} are given, we scale the velocity in terms of the ion Alfvén speed c_{Ai} at the outer boundary $x = 1$, thus introducing the Alfvén crossing time of Table 1. We have

$$c_{Ai} = 2.2\times10^{11}\frac{B}{(\mu_i n_n x_i)^{1/2}}\ [\mathrm{cm\ s^{-1}}]. \tag{30}$$

The corresponding crossing time is

$$\tau_{\rm A} = 0.46\,L_{\rm pc}\frac{(\mu_i n_n x_i)^{1/2}}{B}\ [\mathrm{yrs}]. \tag{31}$$

2.2.5. The inductive time scale τ_{ind}

The inductive time τ_{ind} plays a special role. Unlike the other time scales, it is not a free parameter, but acts as an eigenvalue of the set of ODEs (14 - 16), allowing us to impose four instead of three boundary conditions. We define the inductive time by the scaled electric field

$$\tau_{ind} \equiv \mathcal{E}^{-1} = \frac{LB_0}{cE}. \tag{32}$$

2.2.6. The length scale L

We have not specified the length scale L in equations (22) and (24). It is controlled in part by the global setup of the problem, but is governed by certain constraints. We require L to be small enough that the neutrals are decoupled from the magnetic field, but large enough that the ion-neutral collision time ν_{in}^{-1} is shorter than the local ion dynamical time. In the subsequent discussion, we leave L unspecified, in order to keep the argument as general as possible. In §5 we discuss the physical systems where we believe the combination of ambipolar diffusion and reconnection to be relevant. Table 3 contains characteristic numbers for diffuse clouds, dense clouds, cores and protoplanetary disks. The numbers demonstrate the disparity of time scales in the problem.

2.3. Zero Ion Pressure Gradient

If there is no ion pressure gradient, the dynamics are extremely simple, and serve as a reference to which more general solutions can be compared. This limit is achieved in the case $\beta \equiv 0$ and/or in the case $\tau_i \equiv 0$. We refer to this solution as the pure ambipolar diffusion (AD) solution.

According to equation (15)

$$v = \frac{\tau_A}{\tau_{AD}}\, b\frac{\partial}{\partial x} b \equiv v_{AD}. \tag{33}$$

With equation (33), the magnetic induction equation (14) can be integrated to yield

$$\frac{1}{3\tau_{AD}} b^3 + \frac{1}{\tau_\Omega} b = \frac{x}{\tau_{ind}} + C. \tag{34}$$

Since $b = 0$ at $x = 0$, the constant of integration C must be zero. Using the boundary condition $b(1) = 1$ and assuming $\tau_\Omega \gg \tau_{AD}$, we get for the scaled electric field its AD-solution, namely

$$\frac{cE}{LB_0} = \frac{1}{\tau_{ind}} = \frac{1}{3\tau_{AD}}. \tag{35}$$

Thus, under the conditions of pure AD, with $\lambda_\Omega/\lambda_{AD} \ll 1$, E is independent of λ_Ω, so reconnection is fast.

Equation (34) predicts that the solution has a boundary layer near $x = 0$. Far from the origin,

$$\begin{aligned} b_{AD} &\approx x^{1/3} \\ v_{AD} &\approx -\frac{\tau_{\rm A}}{3\tau_{AD}} x^{-1/3}. \end{aligned} \tag{36}$$

Near the origin,

$$\begin{aligned} b_{AD} &\approx \frac{\tau_\Omega}{3\tau_{AD}} x \\ v_{AD} &\approx -\frac{\tau_A}{\tau_{AD}} \left(\frac{\tau_\Omega}{3\tau_{AD}}\right)^2 x. \end{aligned} \tag{37}$$

Equation (36) holds for $x > x_{AD}$, where

$$x_{AD} \equiv \left(\frac{3\tau_{AD}}{\tau_\Omega}\right)^{3/2}. \tag{38}$$

For $x < x_{AD}$, the solution is given by equation (37).

As equations (36) and (37) show, the flow speed increases toward the origin, then plunges to zero. Thus, in the linear region, the ions are subject to tremendous compression, raising the possibility of strong deceleration of the flow by the ion pressure gradient. In order to see how this limits the rate of reconnection, we consider the role of ion pressure.

2.4. The Effect of Ion Pressure

As long as $\beta \ll 1$, and $\tau_\Omega \ll \tau_{AD}$, ion pressure and resistivity are important only within a boundary layer defined by $x < x_l$. Regularity requires $v \propto x$ as $x \to 0$, and so we introduce a dynamical time τ_d such that

$$v = -\frac{\tau_{\rm A}}{\tau_d} x, \tag{39}$$

for $x < x_l$.

Equation (39) permits us to solve the continuity equation (16) for the central density $r(0) \equiv r_m$. The result is

$$r_m = \frac{\tau_i}{2\tau_d} + \left[1 + \left(\frac{\tau_i}{2\tau_d}\right)^2\right]^{1/2}. \tag{40}$$

We expect $r_m > 1$, for large τ_Ω even $r_m \gg 1$, so that we can write

$$r_m \approx \frac{\tau_i}{\tau_d} \tag{41}$$

We now take the opportunity to correct an error in BZ95. Symmetry considerations require that the Taylor series for $r(x)$ contains only even powers of x: $r(x) = r_m + r_2 x^2 + ...$, while the Taylor series for $v(x)$ contains only even powers: $v(x) = -\tau_{\rm A} x/\tau_d - v_3 x^3 - ....$ BZ95 solved for r_2

without including v_3. This is incorrect, although their conclusions as to the reconnection rate are not affected in the parameter range they considered.

We derived equations (36) and (37) by setting the constant of integration C in equation (34) equal to zero. Now, however, we are not following this solution all the way to the origin. This allows us to introduce a parameter x_* such that

$$\begin{aligned} b &= \left(\frac{x+x_*}{1+x_*}\right)^{1/3} \\ v &= -\frac{\tau_{\rm A}}{3\tau_{AD}\left(x+x_*\right)^{1/3}\left(1+x_*\right)^{2/3}}. \end{aligned} \quad (42)$$

The scaled electric field is then

$$\mathcal{E} = \frac{1}{3\,\tau_{AD}(1+x_*)}, \quad (43)$$

so x_* is effectively a parameterization of $\mathcal{E}$. For $x_* = 0$ we recover the ambipolar diffusion solution equation (35), and this solution is approximately valid as long as $x_* < 1$.

Our description of the system depends on three parameters which are so far unknown. The first, x_l, is the location of the transition between the inner, resistivity and pressure dominated boundary layer and the outer, inductive region. The second, τ_d, is the dynamical time in the inner layer. The third, x_*, measures the departure of the outer solution from the pure AD solution. We can determine these three parameters, thereby patching together a global solution, by applying three conditions which must connect the inner and outer domains.

First, we assume that at $x = x_l$ the solution changes from inductively dominated to resistively dominated. Equating the left hand side of equation (14) to the second term on the right hand side, and using equation (39), we find

$$x_l = \left(\frac{\tau_d}{\tau_\Omega}\right)^{1/2}. \quad (44)$$

As the second condition, we assume continuity of total (plasma plus magnetic) pressure at x_l, and also that magnetic pressure dominates for $x > x_l$ while plasma pressure dominates for $x < x_l$. Our picture is that the plasma pressure profile inside $x = x_l$ is quite flat. These assumptions together, along with equations (15) and (42), lead to

$$\beta\, r_m^\gamma = \left(\frac{x_l + x_*}{1+x_*}\right)^{2/3}. \quad (45)$$

Finally, we postulate mass flux conservation across x_l. Using equations (39) and (42), we have

$$\frac{x_l}{\tau_d} r_m = \frac{1}{3\tau_{AD}\left(x_l+x_*\right)^{1/3}\left(1+x_*\right)^{2/3}}. \quad (46)$$

Eliminating τ_d in equation (41) with equation (44) yields

$$r_m = \frac{\tau_i}{\tau_\Omega x_l^2}. \quad (47)$$

Equation (47) together with equations (46) and (45) leads to a pair of equations for x_l and x_*:

$$x_l^{2\gamma}(x_l+x_*)^{2/3}(1+x_*)^{-2/3} = \beta\left(\frac{\tau_i}{\tau_\Omega}\right)^\gamma \quad (48)$$

$$x_l^3(x_l+x_*)^{-1/3}(1+x_*)^{-2/3} = \frac{3\tau_i\tau_{AD}}{\tau_\Omega^2} \quad (49)$$

It turns out that $x_l/x_* \ll 1$ for all solutions of equations (48) and (49). Therefore, we can approximate equations (48) and (49) by

$$x_l^{2\gamma} x_*^{2/3}(1+x_*)^{-2/3} = \beta\left(\frac{\tau_i}{\tau_\Omega}\right)^\gamma \quad (50)$$

$$x_l^3 x_*^{-1/3}(1+x_*)^{-2/3} = \frac{3\,\tau_i\,\tau_{AD}}{\tau_\Omega^2}. \quad (51)$$

Raising equation (50) to the power $3/(2\gamma)$ and dividing by equation (51) yields an equation for x_* alone

$$x_*^{\frac{3+\gamma}{3\gamma}}\left(1+x_*\right)^{\frac{2\gamma-3}{3\gamma}} = Z^{1/2}, \quad (52)$$

where

$$Z \equiv \beta^{3/\gamma}\frac{\tau_i\tau_\Omega}{9\tau_{AD}^2}. \quad (53)$$

According to this analysis, Z is the fundamental parameter which controls the properties of the layer. When $Z \ll 1$, $x_* \ll 1$ as well, and equation (52) has the approximate solution

$$x_* \approx Z^{\frac{3\gamma}{6+2\gamma}} \ll 1. \quad (54)$$

When $Z \gg 1$, $x_* \gg 1$, and equation (52) yields

$$x_* \approx Z^{1/2} \gg 1. \tag{55}$$

Equations (54) and (55) agree closely when $\gamma = 5/3$, in which case the exponent in equation (54) is $15/28 \approx 0.54$. However, it is useful for comparison with numerical work to find solutions of equations (50) and (51) which are valid for all $x_* \gg x_l$. Dividing equation (50) by equation (51), we get

$$x_l^{2\gamma-3} x_* = \frac{\beta}{3} \frac{\tau_i^{\gamma-1} \tau_\Omega^{2-\gamma}}{\tau_{AD}} \equiv Q. \tag{56}$$

We can express x_* as

$$x_* = Q x_l^{3-2\gamma} \tag{57}$$

and with equation (50) arrive at

$$x_l^{3+\gamma} \left(1 + Q x_l^{3-2\gamma}\right)^{-1} = \left(\beta \left(\frac{\tau_i}{\tau_\Omega}\right)^{\gamma}\right)^{3/2} Q^{-1}. \tag{58}$$

Equation (58) can be solved numerically for x_l, with x_* determined from equation (57). The results are shown in Figure 3 for parameters taken from the series of numerical models $\mathcal{A}$ listed in Table 4.

It is also useful to have approximate analytical expressions for the boundary layer width x_l in the limiting cases $Z \ll 1$, $Z \gg 1$. With equations (50) and (54) we find

$$x_l = \left(9\beta \frac{\tau_i^{\gamma+2} \tau_{AD}^2}{\tau_\Omega^{\gamma+4}}\right)^{1/(6+2\gamma)} \tag{59}$$

for $Z \ll 1$. Using equations (50) and (55) we have

$$x_l = \left(\beta^{1/\gamma} \frac{\tau_i}{\tau_\Omega}\right)^{1/2} \tag{60}$$

for $Z \gg 1$.

Finally, we use equation (43) to derive the scaling of the electric field E with magnetic diffusivity λ_Ω. For simplicity we assume $x_* = Z^{1/2}$ for all Z. We find

$$\frac{d \ln \mathcal{E}}{d \ln \lambda_\Omega} = \frac{\sqrt{Z}}{2(1+\sqrt{Z})}. \tag{61}$$

For $Z \gg 1$, $\mathcal{E} \propto \lambda^{1/2}$, as in Parker-Sweet reconnection, and for $Z \ll 1$ we expect $\mathcal{E} \propto \lambda^0$, i.e. "fast" reconnection.

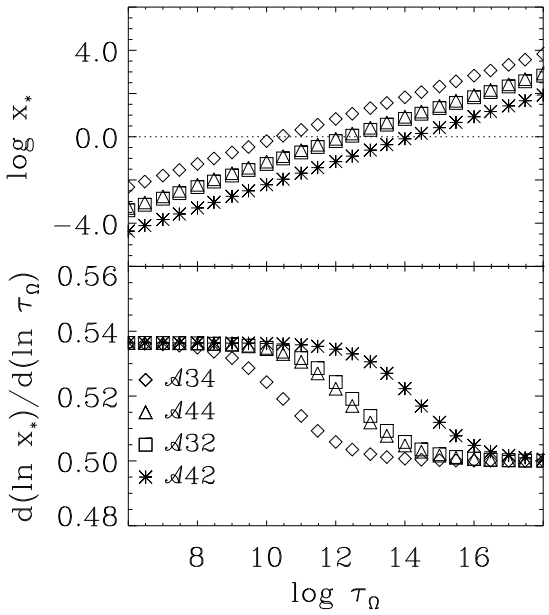

Fig. 3.— x_* against τ_Ω for the general solution of eqn. (58). The exponent change connects the regimes $x_l \ll x_* \ll 1$ and $x_l \ll 1 \ll x_*$.

3. Numerical Method

We seek a numerical solution of the three coupled ODEs (14) - (16). As we mentioned below equation (12), we require that the three dependent variables b, r and v satisfy four boundary conditions (BCs):

$$b(0) = 0 \tag{62}$$

$$v(0) = 0 \tag{63}$$

$$b(1) = 1 \tag{64}$$

$$r(1) = 1 \tag{65}$$

The first two conditions follow from symmetry arguments, and the second two from our characterization of the equilibrium state far from the resistive layer. Note that we do not specify $v(1)$, leaving it free to adjust to the varying resistivity.

Equations (14) - (16) together with conditions (62) - (65) constitute a two-point boundary value problem which is also an eigenvalue problem for $\mathcal{E}$. We implement the constraint on $\mathcal{E}$ by introducing a fourth equation

$$\frac{\partial}{\partial x} \mathcal{E} = \frac{\partial}{\partial x} \frac{\tau_\Omega}{\tau_{ind}} \equiv 0. \tag{66}$$

We solve the problem using a combination of

shooting and relaxation techniques (Press et al. 1992)

The shooting method is based on treating the problem as an initial-value problem with boundary conditions implemented only at $x = 0$. Of N boundary conditions, let n_1 be imposed at $x = 0$ and $n_2 = N - n_1$ BCs at $x = 1$. Thus, for the initial-value problem, we have n_2 freely specifiable parameters at $x = 0$. Outward integration results in values of r, v and b at $x = 1$ which probably do not fit the corresponding BCs. We zero the differences via Newton-Raphson root finding and thus find corrections to the n_2 free values at $x = 0$. The process is repeated until the differences at $x = 1$ are below a given threshold.

The relaxation method uses a finite-difference approximation of the ODEs on a grid with given number of grid points. It too is based on a Newton root-finding scheme (Press et al. 1992). We use the scheme in its simplest form, coupling two neighboring grid points. Higher order coupling is possible, but renders the method much more complex.

The relaxation method requires an initial guess over the full domain for all variables. Thus, we combined both solvers, using the shooting method to obtain an initial guess for the relaxation.

The length scales and time scales in this problem vary over large ranges. For example, the ratio $\tau_\Omega/\tau_{AD} \approx 10^{10}$ for physically realistic parameters. Therefore, our set of ODEs is very stiff. Neither the standard shooting method nor the relaxation method can solve the equations for such parameters. We resolve the problem with a threefold approach.

First – as the most obvious measure – we use a non-uniform grid. The standard solution would be a logarithmic grid, however, the normalization $x(N) = 1$ comes naturally with an exponential grid

$$x(k) = e^{\delta(k-N)}. \tag{67}$$

N is the number of grid points, k the grid point index, and δ a compression factor. The boundary conditions (eq. 62–65) require $b(0) = 0$ and $v(0) = 0$. As we cannot reach $x = 0$ with equation (67), we interpolate linearly between a cutoff x_{cut} and $x = 0$. We choose x_{cut} such that we do not lose any resolution in physically interesting regions.

Second, we approach physically realistic parameters from an initial guess by taking small steps in parameter space. For the $\mathcal{A}$ series of runs, we began with unrealistically small values of τ_Ω and advanced slowly to more realistic values.

Finally, we found that at large τ_Ω or small β the density and velocity gradients are so steep that we can resolve them with the exponential grid only by using an enormous number of grid points, far more than are needed over most of the domain. Accordingly, we introduced a simple version of adaptive mesh refinement. We refine on the velocity difference between two adjacent grid points, $\Delta v_k = |v_k - v_{k-1}|$. If $\Delta v_k > \Delta v_+$ for $k_1 < k < k_2$, the number of grid points in this region is multiplied by $n_+ = 8$. If $\Delta v_k < \Delta v_-$ for $k_1 < k < k_2$ under the condition $k_2 - k_1 > n_-$, the number of grid points in this region is divided by $n_- = 8$. We do not allow refinement or coarsening at the lower and upper boundaries, which in any case is unnecessary. Moreover, refinement is not allowed for

$$\frac{x_k - x_{k-1}}{x_{k-1}} \leq \epsilon_{mach}, \tag{68}$$

where ϵ_{mach} is the machine accuracy. The x-grid is interpolated linearly on the new grid points. The number of gridpoints N typically varies between 10^4 and 3×10^5.

Convergence to a stable solution depends crucially on the overall error criterion. We enforce the fractional error $\epsilon_{conv} \equiv \Delta y/y < 10^{-4}$ for all gridpoints, where y is any of the physical variables b, r, v and $\mathcal{E}$. In order to ensure that we find the correct solution for each parameter adaption iteration, the successive change of a parameter, e.g. τ_Ω, must lead to differences in the results larger than the convergence error ϵ_{conv}. Thus, ϵ_{conv} needs to be adapted with decreasing parameter adaption step size.

We have confirmed that the solution remains independent of N, as long as N is large enough for the relaxation method to converge. The critical region is near the edge of the boundary layer. Solutions for different N are identical within the convergence error ϵ_{conv}. The method develops oscillations in the density around $x \lesssim 1$ with $r/r_{exact} \leq \epsilon_{conv}$, but the overall solution is not affected.

4. Results

We first describe the basic properties of the solutions and discuss the differences between simulations and analytical predictions. Covering a range of 8 orders of magnitude in τ_Ω, we then can infer scaling laws from the simulations and compare them to the predictions.

In order to investigate the dependence of the scaling relations on τ_i and β, we ran models $\mathcal{A}$ within four parameter sets, which are listed in Table 4.

4.1. Basic Properties of the Solutions

Figure 4 shows the full domain for all models of type $\mathcal{A}$ at $\tau_\Omega = 10^{11}$. Gas is moving inwards, i.e. to small x, at approximately constant velocity, until it is brought nearly to a halt by the rapidly increasing plasma pressure at x_l. The magnetic field and the velocity are approximately linear within the boundary layer, as expected from equations (37), but essentially flat in the ambipolar or inductive regime. From equations (36) we would expect $b \propto x^{1/3}$ and $v \propto x^{-1/3}$. Only for model $\mathcal{A}42$ do we notice a slight hint of such behavior. However, in Figure 5, the overplotted outer solutions of equations (36) fit perfectly to the numerical results. The fractional differences between the numerical and analytical solutions at the transition point between the resistive and inductive region amounts to

$$\left|\frac{b_{AD} - b_{sim}}{b_{AD}}\right| \approx \left|\frac{v_{AD} - v_{sim}}{v_{AD}}\right| \approx 10^{-4} = \epsilon_{conv}, \tag{69}$$

where the subscripts AD and sim denote the outer (eqs. 36) and simulation's solution. We realize that the solutions are so flat because, aside from a small region around $x = 1$, we have $x_* \gg x$ for all models except $\mathcal{A}42$ (see Figure 3).

The analytical prediction of the reconnection rate (§2.4) is derived assuming pressure balance between magnetic and ion pressure (eq. 45) and conservation of mass flux across the transition layer (eq. 46). Figure 6 confirms these assumptions. Note that the mass flux scale in the lower panel is linear, while the velocity scale in Figure 4 is logarithmic. While the velocity jumps over nearly two orders of magnitude within $\Delta x \approx 10^{-7}$, the mass flux changes at most by a factor of nearly 4 over at least one order of magnitude in x.

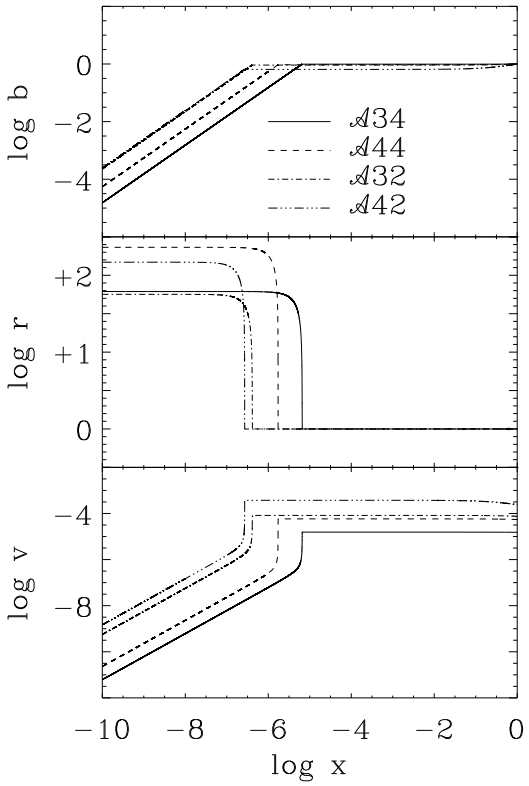

Fig. 4.— Magnetic field b, density r and velocity v at $\tau_\Omega = 10^{11}$. The resistive and ambipolar diffusion regimes are separated by a sharp transition.

The analysis in §2.4 takes the inductive and resistive contributions $\mathcal{E}_{ind}$ and $\mathcal{E}_{res}$ to $\mathcal{E}$ to be equal at x_l, and also uses the assumed linearity of v and b with x. Figure 7 shows x_l *vs* τ_Ω and $d(\ln x_l)/d\ln\tau_\Omega$ *vs* τ_Ω for the $\mathcal{A}$ simulations and for the corresponding analytical predictions. The values of x_l in the simulations can be measured accurately and unambiguously to three significant digits from the first or second derivatives of any of the variables b, r and v. The predicted values of x_l are derived from equation (58). The upper panel of Figure 7 shows a persistent offset between the simulated and predicted values x_l^{sim} and x_l^{pre}, in the sense that x_l^{sim} is always less than x_l^{pre}, sometimes by more than an order of magnitude. As the lower panel of Figure 7 makes clear, the slopes of the $x_l(\tau_\Omega)$ relations differ as well, although $d(\ln x_l)/d(\ln\tau_\Omega)$ computed from the simu-

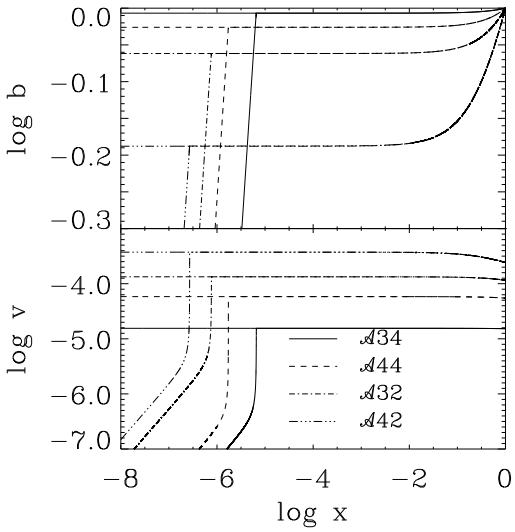

Fig. 5.— Magnetic field b and velocity v at $\tau_\Omega = 10^{11}$. Thick lines: numerical solution, thin lines: outer solution according to equations (36).

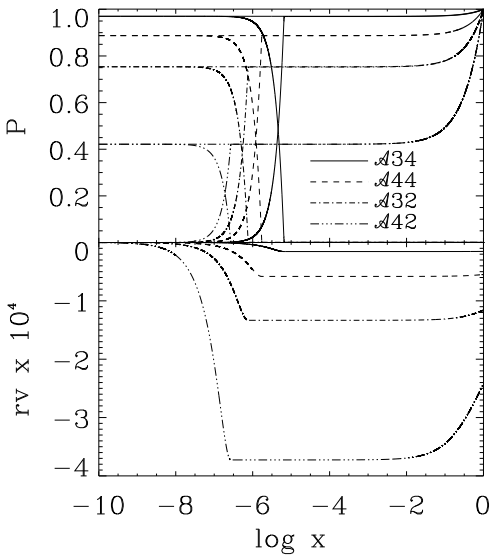

Fig. 6.— *Upper panel*: Magnetic and ion pressure, and their sum for all models at $\tau_\Omega = 10^{11}$. Magnetic and ion pressure add up to a flat curve across x_l. For $x > 10^{-2}$, the magnetic pressure is balanced by the third term in equation 10. *Lower panel*: Mass flux for all models as above. Compared to the corresponding change in velocity (up to two orders of magnitude), the mass flux is nearly constant at x_l.

lations converges to the predicted value of 0.5 for large τ_Ω.

In order to understand this discrepancy, we note that as long as v is given by equation (39),

$$x_l^2 = \frac{\mathcal{E}_{ind}}{\mathcal{E}_{res}} \frac{\tau_d}{\tau_\Omega} \frac{d\ln b}{d\ln x}, \tag{70}$$

where all quantities on the right hand side are evaluated at x_l. Equation (70) reduces to equation (44) for $\mathcal{E}_{ind}/\mathcal{E}_{res} = 1$ and $d(\ln b)/d(\ln x) = 1$.

Examination of $d(\ln b)/d(\ln x)$ in our solutions shows that it drops sharply as $x \to x_l$. With the diminished importance of the resistive term, $\mathcal{E}_{ind}/\mathcal{E}_{res} = 1$ at x_l actually exceeds unity for most runs. However, db/dx is steeper in the inner parts of the layer than it would be if $d(\ln b)/d(\ln x)$ were equal to one throughout. This effectively makes the layer thinner than equation (44) predicts.

4.2. Reconnection Rates

The electric field determines the magnetic reconnection rate (eq. 7), and thus the magnetic energy dissipation rate per volume $\dot{e}_{mag}$ (eq. 8). BZ95 implicitly argued for $E \propto \lambda_\Omega^0$, or $\dot{e}_{mag} \propto \lambda_\Omega^{-1}$, meaning fast reconnection. They used $40 \leq \tau_\Omega/\tau_{AD} \leq 4 \times 10^3$, resulting in a range $4 \times 10^{-3} \leq Z \leq 4 \times 10^1$. Thus, they were well within the fast reconnection regime. However, they assumed isothermality, leading to higher ion densities in the resistive layer.

In the previous section we saw that the scaling for x_l changes at $x_* \approx 1$. As Figure 8 demonstrates, this extends to the electric field scaling. The 8 orders of magnitude in τ_Ω cover the "fast" regime with $\mathcal{E}$ independent of τ_Ω and the "slow" regime with $\mathcal{E} \propto \tau_\Omega^{-1/2}$ or equivalently $\mathcal{E} \propto \lambda_\Omega^{1/2}$ (lower panel of Fig. 8). Both regimes exist. Whether they are both equally realistic, we will discuss in §5.

The lower panel of Figure 8 shows that the scaling of $\mathcal{E}$ with λ_Ω approaches the predicted $\mathcal{E} \propto \lambda_\Omega^{1/2}$ at large τ_Ω. However, there are two discrepancies between the simulations and the theory. First, the value of $\mathcal{E}$ predicted by the analytical theory is always larger than the value found in the simulations. Second, the lower panel shows that the predicted value of τ_Ω at which the reconnection rate changes from fast to slow is larger than the simulated value.

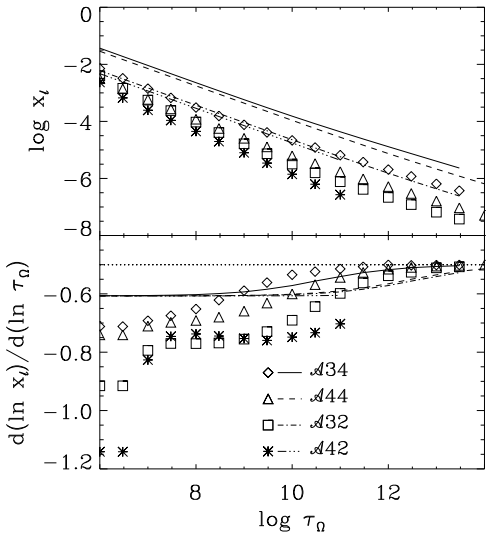

Fig. 7.— *Upper panel*: Resistive scale x_l against resistive time τ_Ω, predicted (lines) according to equations 50 and 51, and determined from the simulations (symbols). *Lower panel*: Exponent q of $x_l \propto \tau_\Omega^q$. The dotted line denotes $q = -0.5$, the theoretical value for $x_* \gg 1$.

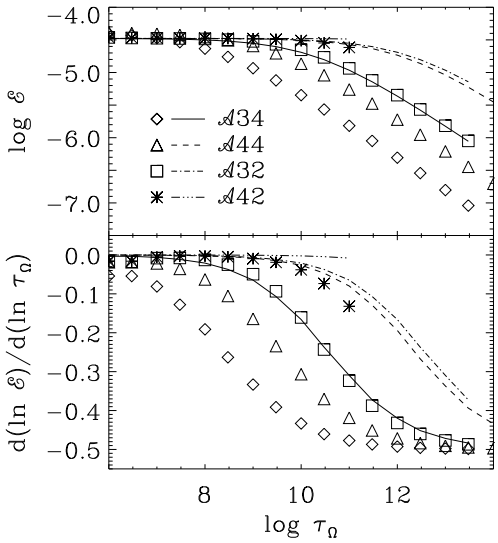

Fig. 8.— Electric field $\mathcal{E}$ against resistive time τ_Ω for all models. Lines represent theoretical predictions, symbols stand for simulations. The lower panel shows the exponent p as in $\mathcal{E} \propto \tau_\Omega^p$.

In the previous subsection, we asserted that two of the key assumptions of the analytical theory - overall pressure balance across the layer, and conservation of mass across the transition - are validated by the simulations. The third assumption, equation (44), is not as well supported because of the flattening of b with x in the outer parts of the layer. This leads to an overestimate of x_l relative to the simulations.

Much of the discrepancy between $\mathcal{E}_{sim}$ and $\mathcal{E}_{pre}$ can be traced to the overestimate of x_l in the analytical theory (fig. 9). Symbols denote $\mathcal{E}_{sim}/\mathcal{E}_{pre}$ for the $\mathcal{A}$ sequence models. Lines stand for the same quantity with the predicted x_l replaced by x_l from the simulations. It is clear that the agreement between theory and simulation is much better in the lower panel.

Theory and simulation agree significantly better for series $\mathcal{A}32$ and $\mathcal{A}42$ than for series $\mathcal{A}34$ and $\mathcal{A}44$ (figs. 8 and 9). In the first two series of models, the inequality

$$\tau_i \ll \tau_{AD} \ll \tau_\Omega \tag{71}$$

is well satisfied, while for the other two series it is not.

In summary, we see a reasonable degree of consistency between the simulations and the analytical theory. Based on their agreement, we are confident that the theory identifies the important physical effects, while the simulations provide numerical factors which correct the theory.

According to the theory, the reconnection rate is determined by the parameter Z defined in equation (53). Figure 10 shows $\mathcal{E}$ and $d\ln\mathcal{E}/d\ln Z$ plotted against Z for all the $\mathcal{A}$ series simulations (the usual symbols) and for the theory, shown as a solid line. The first observation is that Z is indeed a good parameter for ordering the results of the simulations. While the simulations do not fall onto a single curve because of the effects discussed above (e.g. eq. 71), they lie quite close together. The analytical predictions for different models are of course indiscernible. We see also that reconnection slows down at a smaller value of Z than predicted by the theory. Empirically, we suggest $Z \approx 0.01$ rather than $Z = 1$ as the dividing line. We identified the discrepancies between predictions and simulations as being caused by the over-idealized linearity of b and v for $x < x_l$. Thus, we will use the analytical predictions for the subsequent discussion, but correct them by replacing Z by $100\,Z$.

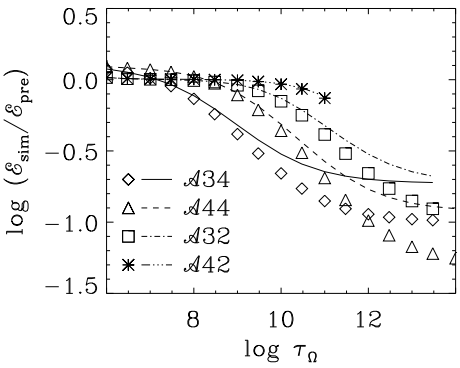

Fig. 9.— Ratio of simulated over predicted electric field $\mathcal{E}$ against resistive time τ_Ω for all models. The agreement between theory and simulation deteriorates for large →. Symbols denote $\mathcal{E}_{sim}/\mathcal{E}_{pre}$, lines stand for the same quantity with the predicted x_l replaced by x_l from the simulations.

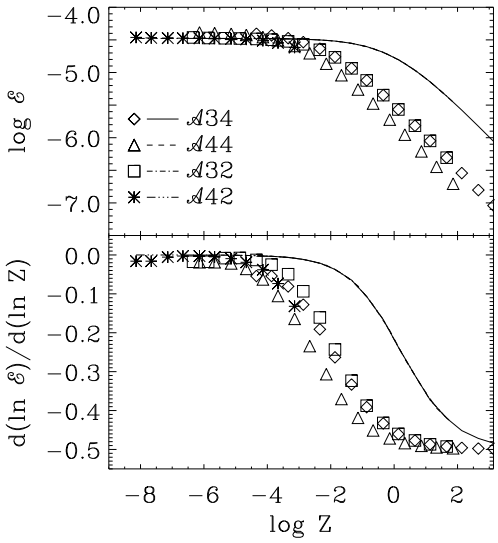

Fig. 10.— Electric field $\mathcal{E}$ against scaling parameter Z as defined in equation (53).

5. Physical Interpretation

We now apply our results to weakly ionized astrophysical environments. We begin by discussing the choice of length scale L. Then we derive the reconnection rate as a function of L for some astrophysical systems of interest. We estimate the rate of Ohmic heating and show that it is extremely high within the resistive layers. Finally, we discuss the implications for the ISM and for protoplanetary disks.

5.1. The Choice of L

One crucial parameter has yet to be defined: the length scale L of the domain (see §2.2.6). The scaling parameter Z – and thus the reconnection rate – depends on L as L^{-2}. Thus, we predict faster reconnection in smaller systems, which is intuitively plausible.

In order for the set of equations (9) - (11) to be valid, the ions and neutrals must move independently of one another. To estimate the length scale at which this occurs, we consider small perturbations of the two fluid system having wave number k perpendicular to the magnetic field. In the limit $k \to 0$, the ions and neutrals are almost perfectly coupled. As k increases, the coupling decreases, until $\mid (v_i - v_n)/v_i \mid \sim 1$ at a wavenumber k_D which is given by

$$k_D = \frac{2\nu_{ni}}{c_{An}} \left(1 + \frac{c_{sn}^2}{c_{An}^2}\right)^{1/2}. \tag{72}$$

Thus, we require $L \leq 2\pi/k_D \equiv L_{AD}$. For small c_{sn}/c_{An}, equation (72) reverts to the usual result for hydromagnetic waves (e.g Ferrière et al. (1988)). If c_{sn}/c_{An} is large, as we might expect in the vicinity of a neutral sheet, the critical scale is smaller by a factor of c_{An}/c_{sn}.

L_{AD} can also be defined in terms of the ambipolar Reynolds number R_{AD} (Zweibel & Brandenburg 1997; Klessen et al. 2000)

$$R_{AD} = \frac{Lv}{\lambda_{AD}}, \tag{73}$$

where λ_{AD} is defined in equation (23) and v is the speed of the neutrals. Then, L_{AD} is the value of L for which $R_{AD} = 1$. If we replace v by the magnetosonic speed $(c_{An}^2 + c_{sn}^2)^{1/2}$, then $L_{AD} \approx k_D^{-1}$. However, equation (73) also allows for the possibility that the system is dominated by supermagnetosonic flows. It is possible that L could be less than L_{AD} if it were defined by a geometrical property of the system, such as the thickness of an accretion disk. However, L cannot be greater than L_{AD} if the equations we solved are to be valid.

The requirement that the system be collisional

gives a lower limit for L, namely

$$L > L_{col} \equiv c_{si}/\nu_{in}, . \tag{74}$$

where $\nu_{in} \equiv \mu_n n_n \langle\sigma v\rangle/(\mu_i + \mu_n)$ is the ion-neutral collision frequency.

5.2. Reconnection Rates in Physical Environments

Table 3 lists representative values of physical parameters in four environments: (a) diffuse clouds, (b) dense molecular clouds, (c) molecular cores and (d) protoplanetary disks. In Figure 11 we plot the incoming ion flow speed – the reconnection rate – in units of the neutral Alfvén speed c_{An} against the scale length.

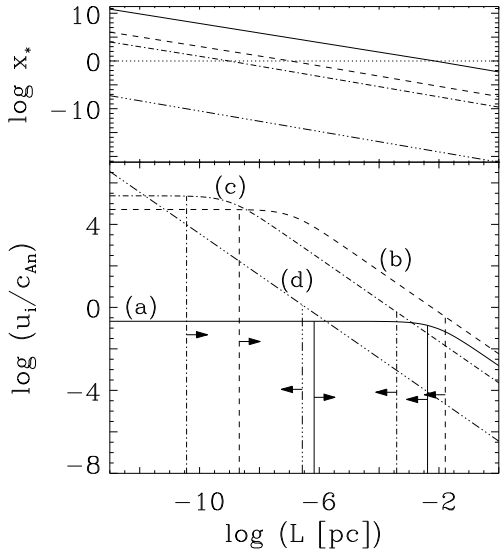

Fig. 11.— Scaling parameter x_* and reconnection rate u_i in units of the neutral Alfvén speed c_{An} against domain scale for the parameter sets (a), (b), (c) and (d) as defined in Table 3. The vertical lines denote the constraints on L discussed in §5.1, and right (left) pointing arrows stand for lower (upper) thresholds, according to equations (73) and (74). We use the empirical formula $x_* = 10Z^{1/2}$.

At small L, the curves reach a saturated, maximum value u_{is}. Using eqns. (42) and the upper panel of Figure 11, we see that this saturated velocity is

$$u_{is} = \left(\frac{\lambda_\Omega}{\tau_i\,\beta^{3/\gamma}}\right)^{1/2}. \tag{75}$$

At large L, eqns (42) show that u_i is given approximately by $\lambda_{AD}/3L$. However, only the part of the domain with $L_{col} < L < L_{AD}$ is accessible for any given environment. These limits are marked on each of the curves.

Figure 11 shows that magnetic fields can merge quite rapidly under realistic astrophysical conditions. Note that the reconnection speed u_{is}, which is the maximum reconnection speed as a function of L with all other parameters held fixed, actually corresponds to *slow* reconnection in the sense we originally defined it: $u_{is} \propto \lambda_\Omega^{1/2}$. However, u_{is} is generally much faster than the Parker-Sweet reconnection speed u_z defined in equation (4). Using equations (6) and (75), we see that

$$\frac{u_{is}}{u_z} = \frac{\tau_A}{\tau_i \beta^{3/\gamma}}, \tag{76}$$

where τ_A is to be computed using the total mass density. The relative rapidity of magnetic merging comes about because the recombination time is short compared to the flow time along the neutral sheet, and the plasma β is very small.

5.3. Ohmic Heating

If any aspect of magnetic merging of the type described here is observable, it is likely to be related to Ohmic heating. In a steady state, the flux of magnetic energy into the layer is balanced by radiation, resulting in a radiative flux F_r of

$$F_r = 2u_i \frac{B_0^2}{4\pi}. \tag{77}$$

The spectrum of the emergent radiation depends on the temperature in the layer. While a full thermal equilibrium model is beyond the scope of this paper, it is useful to calculate the Ohmic heating rate. At the midplane, according to equations (8) and (43), the energy dissipation rate per unit volume is

$$\dot{e}_{mag} = \frac{B_0^2}{4\pi\,\tau_i\,\beta^{3/\gamma}} \frac{Z}{(1+x_*)^2}. \tag{78}$$

Recalling that $x_* \sim Z^{1/2}$, we see that equation (78) predicts that $\dot{e}_{mag} \propto L^{-2}$ for $x_* \ll 1$ and reaches a saturated value of $B_0^2/(4\pi\,\tau_i\,\beta^{3/\gamma})$ for $x_* \gg 1$. We have evaluated $\dot{e}_{mag}$ for the models in series $\mathcal{A}$. It is nearly constant at the midplane value throughout the inner boundary layer,

and plunges to very small values outside it. Figure 12 shows the boundary layer magnitudes of $\dot{e}_{mag}$ as a function of L for the four environments listed in Table 3, with the permitted range of L values indicated in each case. The dependence on L follows the prediction of equation (78).

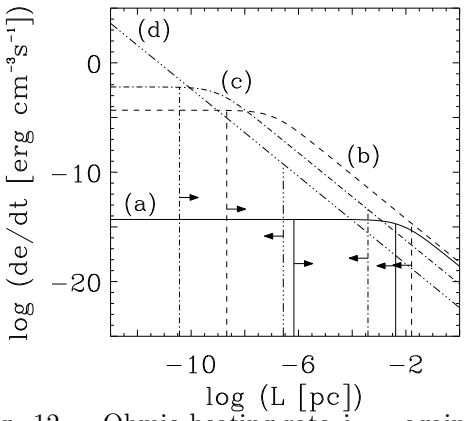

Fig. 12.— Ohmic heating rate $\dot{e}_{mag}$ against scale length L for the parameter sets (a), (b), (c) and (d) as defined in Table 3. Physically relevant regimes are denoted by vertical lines as in Figure 11. We used the empirical result $x_* = 10Z^{1/2}$.

The saturated values of $\dot{e}_{mag}$ in all these environments are extremely large in comparison to the radiative cooling rates. For example, in diffuse clouds [case (a)], the maximum cooling rate by the 158μm fine structure line of C II is 8×10^{-23} ergs cm^{-3} s^{-1}. This implies that the gas is heated to very high temperatures, and perhaps is even thermally ionized. This must slow down the reconnection rate at smaller values of τ_Ω than predicted by our theory. We could very roughly account for the increase in plasma pressure by choosing $\gamma > 5/3$. The theory predicts that as the equation of state stiffens, the reconnection rate slows down and the boundary layer thickens.

The high current density in the boundary layer might destabilize high frequency waves which would provide anomalous resistivity through wave-particle interactions and increase the merging rate. Following the early suggestion by Krall & Liewer (1971), attention focussed on the lower hybrid drift instability as the mechanism for generating the waves. Although it now appears unlikely that drift waves themselves are a source of anomalous resistivity, but they may play a role in the growth of Kelvin-Helmholtz instabilities, which change the topology of the reconnection region (Lapenta & Brackbill 2002). Additional sources of small scale turbulence in null layers could also contribute to anomalous resistivity (Ozaki et. al. 1996).

Although the heating is intense, the narrowness of the layers is a formidable barrier to their direct detectability. The analytical formulation predicts that the dimensional layer width, Lx_l, scales as $L^{3/14}$ for $Z \ll 1$ and is independent of L for $Z \gg 1$; $Lx_l \sim (\beta^{1/\gamma}\, \tau_i\, \lambda_\Omega)^{1/2}$. The layer widths are plotted in Figure 13 for the four environments listed in Table 3.

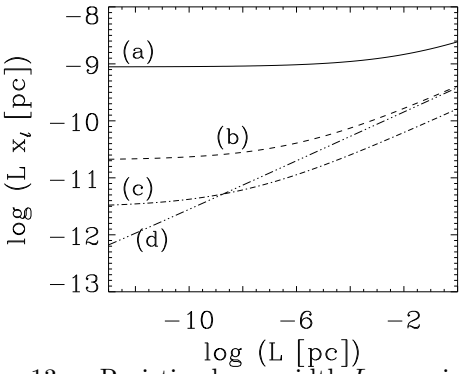

Fig. 13.— Resistive layer width Lx_l against scale length L for the parameter sets (a), (b), (c) and (d) as defined in Table 3. At $x_* \approx 1$ (see fig. 11), the dependence of x_l on L changes from flat to increasing. We took $x_* = 10Z^{1/2}$

5.4. Reconnection in the ISM and Protoplanetary Disks

Figure 11 allows us to read off the range of lengthscales over which our theory applies, and rates of reconnection predicted by the theory, in a given environment. For the diffuse clouds (a), the reconnection rate saturates at a sub-Alfvénic value of u_{is}. Within the permissible range of length scales – denoted by the vertical solid lines and inward-pointing arrows –, u_i has reached its saturated value u_{is}. Reconnection can occur only if the system survives for a few tens of Alfvén crossing times.

The situation is different for the environments (b) and (c), namely molecular clouds and cloud cores. In both cases, the saturated reconnection

rate u_{is} is super-Alfvénic by several orders of magnitude, and the permissible scale length range extends well into the saturated regime. Even in the unsaturated regime, it is possible to merge at roughly c_{An} if L is a few hundredths to a few thousandths of a parsec. Such scales can be imaged directly, and are known to support density structure. Therefore, reconnection is a viable process for the annihilation of opposing flux systems in molecular clouds.

Protoplanetary disks are much smaller than interstellar clouds, so curve (d) of Figure for $L \lesssim 10^{-3}$ pc. The physically permissible scale lengths range from $\approx 10^{-7}$ pc down to a few meters. The inflow velocity saturates only at the smallest scales, but the flow velocity is super-Alfvénic over approximately 7 orders of magnitude in scale length L. The heating provided by fast reconnection (Fig. 12) points into the direction of models for chondrule formation as discussed by e.g. Levy & Araki (1989), Cameron (1995) and Joung et al. (2002).

6. Summary and Discussion

In this paper, we have determined the rate at which magnetic flux can be supplied to a weakly ionized, neutral layer where it is resistively destroyed under steady state conditions. Through an extensive parameter study, covering 8 orders of magnitude in resistivity, we were able to find the regimes of slow and fast reconnection, and identify the parameter Z (eq. 53) which distinguishes between them. Our simple analytical model and the simulations agree qualitatively. Quantitative agreement follows directly from accounting for the over-idealized linearity of the analytical solution. Thus, we are confident that we can apply our model to astrophysical environments, provided that no additional effects intervene.

Our results generalize and extend BZ95. In §2.4, we pointed out an error in the formulation in that paper. The analysis in BZ95 predicts reconnection at a rate independent of λ_Ω as long as $Z < \beta$, while the analysis here predicts that the rate is independent of λ_Ω as long as $Z < 1$.

Our model is the simplest one possible. The flow is one dimensional, and the magnetic field vanishes at the midplane. Thus, it is worth asking whether the model can be generalized. Two dimensional flow, as in the Parker-Sweet model of reconnection, provides another mechanism for removing ions from the resistive layer. However, we already know that this leads to a slow reconnection rate. Fast reconnection in our model is achieved through a short recombination time, which removes ions more rapidly than outflow at the Alfvén speed. The 2D problem was considered by Vishniac & Lazarian (1999). Their result for the reconnection rate, if Ohmic heating is negligible, is slower than ours by a factor β^{-1}.

If we included a third component of magnetic field, which did not vanish at the neutral line, the modifications would be more substantial. Magnetic pressure from this third component would reduce the flow speed and prevent steepening of the profile. In the case of a dominant third component, we should recover the theory of tearing modes in weakly ionized gas (Zweibel 1989), in which the reconnection rate is enhanced only by a factor of $(\rho/\rho_i)^{1/5}$, and thus remains slow.

Reconnection is also somewhat slowed down in situations where recombination proceeds on grains, and the grains are tied to the neutrals. An analysis similar to that in §2.4 shows that $x_* \approx \beta^{-1/2\gamma} Z^{1/2}$ for $x_* \gg 1$.

Bearing these caveats in mind, fast reconnection – i.e. a reconnection rate independent of λ_Ω – is possible within the model presented. The conditions which must be met are (i) a short ionization time, guaranteeing the fast removal of ions in the resistive layer and thus preventing a pressure build-up, and (ii) a negligible ion pressure in comparison to neutral and magnetic pressure.

As we saw in Figure (11), the maximum merging speed is actually "slow" in the sense that it depends on λ_Ω as $\lambda_\Omega^{1/2}$. Quantitatively, however, it is quite fast: super-Alfvénic for the molecular cloud and protoplanetary disk environments which we considered (cases (b)-(d) of Table 3), and sub-Alfvénic by less than two orders of magnitude for diffuse clouds [case(a)]. We showed that at length-scales less than the ion-neutral decoupling length L_{AD} defined by equation (73), reconnection is indeed in the super-Alfvénic regime. In protoplanetary disks (case (d)), fast reconnection might be a good candidate to supply sufficient heat for chondrule formation. Fundamentally, reconnection is rapid as long as the plasma β is low and the re-

combination time of ions is much less than the flow time at the Alfvén speed.

An extension of the model to higher dimensions and including time dependence seems desirable, in order to test whether the process is indeed influential under more realistic conditions.

We would like to thank M. Haverkorn for comments on the manuscript. Our discussions with M.-M. Mac Low and R. M. K. Joung were very helpful. FH is partially supported by a Feodor-Lynen grant of the Alexander von Humboldt Foundation. The (U.S.) National Science Foundation provided partial support through grants AST-9800616 and AST-0098701.

REFERENCES

Biskamp, D. 1986, Phys. Fluids, 29, 1520

Biskamp, D. 1993, Cambridge Monographs on Plasma Physics, Cambridge University Press

Biskamp, D. 1994, Phys. Rep., 237, 179

Biskamp, D., Schwarz, E., Drake, J. F. 1995, Phys. Rev. Lett., 75, 3850

Braginskii, S. I. 1965, Rev. Plasma Phys., 1, 205

Brandenburg, A. & Zweibel, E. G. 1994, ApJ, 427, L91

Brandenburg, A. & Zweibel, E. G. 1995, ApJ, 448, 734

Cameron, A. G. W. 1995, Meteoritics, 30, 133

Chiueh, T. & Zweibel, E. G. 1989, ApJ, 338, 1158

Ciolek, G.E. & Mouschovias, T. Ch. 1993, ApJ, 418, 774

Cowley, S. W. H. 1975, J. Plasma Phys., 14, 475

Dorman, V. L. & Kulsrud, R. M. 1995, ApJ, 449, 777

Draine, B.T, Roberge, W.G., Dalgarno, A. 1983, ApJ, 264, 485

Draine, B.T. & Sutin, B. 1987, ApJ, 320, 803

Ferrière, K. M., Zweibel, E. G., & Shull, J. M. 1988, ApJ, 332, 984

Forbes, T. G. 2001, Earth Planets Space, 53, 423

Furth, H. P., Killen, J., Rosenbluth, M. N. 1963, *Phys. Fluids*, 6, 459

Joung, R. M. K., Mac Low, M.-M., Ebel, D. 2002, *Icarus*, *in preparation*

Klessen, R. S., Heitsch, F., Mac Low, M.-M. 2000, ApJ, 535, 887

Krall, N.A. & Liewer, P.C. 1971, Phys. Rev., 4, 2094

Kulsrud, R. M. 1998, Phys. Plasmas, 5, 1599

Kulsrud, R. M. 2001, Earth Planets Space, 53, 417

Lapenta, G. & Brackbill, J. U. 2002, Phys. Plasmas, 9, 1544

Levy, E. H. & Araki, S. 1989, Icarus, 81, 74

Mathis, J. S., Rumpl, W., & Nordsieck, K. H. 1977, ApJ, 217, 425

McKee, C.F. 1989, ApJ, 345, 782

Lazarian, A. & Vishniac, E. T. 1999, ApJ, 517, 700

Mandt, M. E., Denton, R. .E., Drake, J. F. 1994, Geophys. Res. Lett., 21, 73

Mestel, L. & Spitzer, L. Jr. 1956, MNRAS, 116, 503

Ozaki, S., Sato, T., Horiuchi, R., & Complexity Simulation Group 1996, Phys. Plasma, 3, 2265

Osterbrock, D. E. 1989, *Astrophysics of gaseous nebulae and active galactic nuclei*, University Science Books

Parker, E. N. 1955, ApJ, 122, 293

Parker, E. G. 1957, J. Geophys. Res., 62, 509

Petschek, A. G. 1964, *The Physics of Solar Flares*, AAS-NASA Symposium, NASA SP-50, ed. W. N. Hess (Greenbelt, Maryland)

Press, W. H., Teukolsky, S. A., Vetterling, W. T., Flannery, B. P. 1992, *Numerical Recipes in C*, Cambridge University Press, 2nd edition

Scholer, M. 1989, J. Geophys. Res., 94, 8805

Sweet, P. A. 1958, *Electomagnetic Phenomena in Cosmical Physics*, Cambrigde University Press

Treumann, R. A. 2001, Earth Planets Space, 53, 453

Ugai, M. 1995, Phys. Plasmas, 2, 388

Uzdensky, D. A. & Kulsrud, R. M. 2000, Phys. Plasmas, 7, 4018

Vishniac, E. T. & Lazarian, A. 1999, ApJ, 511, 193

Zweibel, E. G. 1989, ApJ, 340, 550

Zweibel, E. G. & Brandenburg, A. 1997, ApJ, 478, 563

This 2-column preprint was prepared with the AAS LaTeX macros v5.0.

TABLE 1
PHYSICAL AND DIMENSIONLESS VARIABLES

quantity	physical	dimensionless
length	z	$x = z/L$
ion density	ρ_i	$r = \rho_i/\rho_{i0}$
ion velocity	u_i	$v = u_i/c_{Ai}$
magnetic field	B	$b = B/B_0$
electric field	E	$\mathcal{E} = cE/(LB_0)$

NOTE.—L is the physical domain length, c_{Ai} the Alfvén speed. Note that the scaled electric field is not a dimensionless variable, but the inverse of a time scale. The obvious non-dimensionalization by taking $cEL/(\lambda_\Omega B_0)$ proves to be inconvenient because of the λ_Ω-dependence.

TABLE 2
TIME SCALES USED IN THE DIMENSIONLESS EQUATIONS

timescale	symbol	definition
Ohmic	τ_Ω	L^2/λ_Ω
ambipolar	τ_{AD}	L^2/λ_{AD}
ionization	τ_i	$(R_i\rho_{n0}/\rho_{i0})^{-1}$
recombination	τ_{rec}	$(R_{rec}\rho_{i0})^{-1}$
inductive	τ_{ind}	LB_0/cE
Alfvén	τ_A	L/c_{Ai}

NOTE.—Time scales used in the dimensionless equations (14), (15, (14). The physical variables are defined in Table 1.

TABLE 3
PHYSICAL PARAMETERS AND TIME SCALES

quantity	(a)	(b)	(c)	(d)
$n_n\,[\mathrm{cm}^{-3}]$	10^2	10^4	10^6	10^{13}
μ_n	1.3	2.2	2.2	2.2
μ_i	12	29	29	40
x_i	10^{-4}	10^{-7}	10^{-8}	10^{-12}
$B_0\,[\mathrm{G}]$	10^{-5}	5×10^{-5}	2×10^{-4}	1
$T_n\,[\mathrm{K}]$	80	10	30	500
$c_{si}\,[\mathrm{cm/s}]$	3.0×10^4	6.9×10^3	1.2×10^4	4.1×10^4
$c_{Ai}\,[\mathrm{cm/s}]$	6.3×10^6	6.4×10^7	8.1×10^7	1.1×10^{10}
$c_{sn}\,[\mathrm{cm/s}]$	9.2×10^4	2.5×10^4	4.3×10^4	1.8×10^5
$c_{An}\,[\mathrm{cm/s}]$	1.9×10^5	7.4×10^4	3.0×10^4	4.7×10^4
$\tau_i\,[\mathrm{yr}]$	3.4×10^3	7.6×10^0	2.9×10^{-1}	1.6×10^{-7}
β	4.6×10^{-5}	2.3×10^{-8}	4.3×10^{-8}	2.9×10^{-11}
$r_{gyro}\,[\mathrm{cm}]$	2.6×10^6	2.9×10^5	1.3×10^5	1.2×10^2
$L_{AD}\,[\mathrm{pc}]$	4.2×10^{-3}	1.6×10^{-2}	3.9×10^{-4}	2.7×10^{-7}
$L_{col}\,[\mathrm{pc}]$	6.7×10^{-7}	2.1×10^{-9}	3.6×10^{-11}	1.2×10^{-17}

NOTE.—Parameters for (a) diffuse clouds, (b) dense clouds, (c) cores and (d) protoplanetary disks. $\gamma = c_p/c_v = 5/3$. Molecular weights μ, sound speed c_s and Alfvén velocity c_A refer to the ions or neutrals, depending on their index i or n. The ionization time is given in §2.2.3, and the plasma β refers to the ions. Equations (73) and (74) define L_{AD} and L_{col}. The ion gyroradius $r_{gyro} = c\sqrt{kT\mu_i m_H}/eB$.

TABLE 4
SIMULATION PARAMETERS

Model	β	τ_i	τ_{AD}	τ_A	τ_Ω	Z/τ_Ω
$\mathcal{A}34$	10^{-3}	10^4	10^4	10	*	4.4×10^{-11}
$\mathcal{A}44$	10^{-4}	10^4	10^4	10	*	7.0×10^{-13}
$\mathcal{A}32$	10^{-3}	10^2	10^4	10	*	4.4×10^{-13}
$\mathcal{A}42$	10^{-4}	10^2	10^4	10	*	7.0×10^{-15}

NOTE.—Time scales (in years) and β for the simulations. For all runs of type $\mathcal{A}$ we have $10^6 \le \tau_\Omega \le 10^{14}$, denoted by *. See §2.2.6 for a discussion of the physical regimes covered. The first digit in the model name indicates β, the second τ_i.